Azimuthal elastic impedance inversion for fluid term and fracture weakness

Huaizhen Chen, Kristopher Innanen, Yuxin Ji (SINOPEC), Xiucheng Wei

ABSTRACT

Fracture weaknesses and fluid factor are important parameters to identify the location of underground fractures and the type of fluids. An indirect method to predict fractures and discriminate the fluid is first using azimuthal seismic data to estimate the normal and tangential fracture weaknesses and then calculating the fracture fluid factor. The indirect method may create some uncertainties, and the estimated fracture weaknesses are affected by both the fluid and fractures. We demonstrate a direct method to estimate Lamé constants and fracture weaknesses of the dry fractured rock, and fluid term from partially incident-angle-stack seismic data, based on azimuthal elastic impedance (EI) parameterization and inversion. Combining stiffness parameter perturbations and scattering function, we first derive a linearized PP- wave reflection coefficient for the case of an interface separating two horizontal transverse isotropic (HTI) media, which can isolate the effects of fractures and fluids. Using the derived reflection coefficient, we propose the expression of azimuthal EI. The estimation of fluid term and fracture weaknesses is implemented as a two-step inversion, which includes inversion of partially-incident-stack seismic data for EI at different azimuths, and the estimation of fluid term and fracture weaknesses from the inverted results of azimuthal EI using a Bayesian Markov- chain Monte Carlo (MCMC) method. Tests on synthetic and real data can confirm the stability of the proposed inversion method, and the inversion method appears to be useful for fracture detection and fluid discrimination.

INTRODUCTION

Fracture detection and filling discrimination are important tasks for the unconventional reservoir (shale, tight sand, et al.) characterization. Effect models, including Hudson cracked model (Hudson 1980) and linear slip model (Schoenberg and Douma, 1988; Schoenberg and Sayers, 1995), are defined to describe the effect of cracks and fractures on stiffness and compliance matrices. Bakulin et al. (2000) present relationships between fracture properties (fracture density, fracture aspect ratio, and fillings) and fracture weaknesses for the dry and wet rock. Combining these relationships, Chen et al. (2014a) propose an indirect method to estimate the normal and tangential fracture weaknesses first and then to calculate the fluid factor which is proposed by Schoenberg and Sayers (1995). However, the estimated fracture weaknesses are affected by both the fracture and fluid, and the indirect method may also cause some uncertainties.

A rock, containing a set of vertical or sub-vertical fractures, can be considered as a horizontal transverse isotropic (HTI) medium. Rüger (1997, 1998) derives an approximate expression of PP- wave reflection coefficient in terms of anisotropic parameters for HTI media. Shaw and Sen (2004) present a method to combine a scattering function and stiffness parameter perturbations to derive linearized reflection coefficients for weak anisotropic media. Based on the Rüger equation, many geophysicists utilize amplitude variation with offset and azimuth (AVOA) data to estimate anisotropic parameters (Barchrach et al., 2009;

Downton and Roure, 2010). For real data processing, AVOA data are usually influenced by random noises, and AVOA inversion is also affected by the extracted wavelets, which may reduce the accuracy of fracture prediction. Elastic impedance (EI) is first introduced by Connolly (1998), which is an extension of acoustic impedance (AI). For an isotropic medium, EI varies with offset (the angle of incidence), and for an azimuthal anisotropic medium (or a vertically fractured medium), EI changes with the angle of incidence and azimuth (Martins, 2006). Using partially incident-angle-stack seismic data to invert for azimuthal EI datasets, and then utilizing the inverted azimuthal EI to estimate parameters (P-wave and S- wave impedances and velocities, density, etc.) have been proven as an efficient method for reservoir characterization (Zong et al., 2012; Yin and Zhang, 2014; Chen et al., 2014b).

In the present study, under the assumption of small fracture weaknesses and low-moduli fillings, we first make a simplification of fluid substitution equations in HTI media, based on Gassmann equation and Huang et al. (2015) equation. For the case of an interface separating two HTI media, we derive the approximated perturbation of stiffness parameters. Using the method proposed by Shaw and Sen (2004), we present a linearized PP- wave reflection coefficient in terms of Lamé constants, density, Gassmann fluid term, and the normal and tangential weaknesses, which may isolate the effects of dry rock framework, fluid, and fractures. Based on the derived PP- wave reflection coefficient, we present the expression of azimuthal EI. We demonstrate a method to estimate Lamé constants, density, fluid term, and fracture weaknesses from azimuthal seismic data, which is implemented as a two-step inversion (azimuthal EI inversion from partially incident-angle-stack seismic data using a least- square algorithm, and the extraction of parameters from the inverted results of azimuthal EI using a Bayesian Markov- chain Monte Carlo, MCMC, method). Synthetic tests indicate that Lamé constants, fluid term, and the normal and tangential fracture weaknesses can be estimated reasonably when seismic traces contain a moderate noise. A test on real data from a gas-bearing fractured shale reservoir, demonstrates that the proposed inversion method is efficient for fracture prediction and fluid discrimination.

THEORY AND METHOD

Stiffness parameters of saturated fractured media

An equivalent HTI medium is formed by combining a homogeneous isotropic rock and a system of vertical or sub-vertical parallel fractures. For a dry vertically fractured rock, the stiffness matrix is given by linear-slip theory (Schoenberg and Douma, 1988; Schoenberg and Sayers, 1995)

$$C = \begin{bmatrix} M(1-\Delta_{\rm N}) & \lambda(1-\Delta_{\rm N}) & \lambda(1-\Delta_{\rm N}) & 0 & 0 & 0 \\ \lambda(1-\Delta_{\rm N}) & M(1-\chi^2\Delta_{\rm N}) & \lambda(1-\chi\Delta_{\rm N}) & 0 & 0 & 0 \\ \lambda(1-\Delta_{\rm N}) & \lambda(1-\chi\Delta_{\rm N}) & M(1-\chi^2\Delta_{\rm N}) & 0 & 0 & 0 \\ 0 & 0 & 0 & \mu & 0 & 0 \\ 0 & 0 & 0 & 0 & \mu(1-\Delta_{\rm T}) & 0 \\ 0 & 0 & 0 & 0 & 0 & \mu(1-\Delta_{\rm T}) \end{bmatrix}, \tag{1}$$

where $M = \lambda + 2\mu$, $\chi = \lambda/M$, λ and μ are Lamé constants, and $\Delta_{\rm N}$ and $\Delta_{\rm T}$ are the normal and tangential fracture weaknesses.

The effect of fluid on stiffness matrix parameters of an anisotropic rock is first presented by Gassmann (1951), and Huang et al. (2015) propose a set of equations for fluid substitution in HTI media

$$
\begin{aligned}
C_{11}^{sat} &= (\lambda+2\mu)(1-\Delta_{\mathrm{N}}) + \frac{[K_0 - K_d(1-\Delta_{\mathrm{N}})]^2}{(K_0/K_f)\phi(K_0-K_f)+(K_0+A)},\\
C_{12}^{sat} &= \lambda(1-\Delta_{\mathrm{N}}) + \frac{[K_0 - K_d(1-\Delta_{\mathrm{N}})][K_0 - K_d(1-\chi\Delta_{\mathrm{N}})]}{(K_0/K_f)\phi(K_0-K_f)+(K_0+A)},\\
C_{23}^{sat} &= \lambda(1-\Delta_{\mathrm{N}}) + \frac{[K_0 - K_d(1-\chi\Delta_{\mathrm{N}})]^2}{(K_0/K_f)\phi(K_0-K_f)+(K_0+A)},\\
C_{33}^{sat} &= (\lambda+2\mu)(1-\chi^2\Delta_{\mathrm{N}}) + \frac{[K_0 - K_d(1-\chi\Delta_{\mathrm{N}})]^2}{(K_0/K_f)\phi(K_0-K_f)+(K_0+A)},\\
C_{44}^{sat} &= \mu,\\
C_{55}^{sat} &= \mu(1-\Delta_{\mathrm{T}}),
\end{aligned}
\tag{2}
$$

where $A = K_d(1-\Delta_{\mathrm{N}}K_d/M)$, K_0 is the effective bulk modulus of mineral making up the rock , K_d is the bulk modulus of dry rock, K_f is the bulk modulus of fluid, and ϕ is the total porosity, respectively.

Under the assumption of small fracture weaknesses (the normal and tangential fracture weaknesses are not too large) and low moduli fillings (the moduli of fillings are small), we may make a simplification of stiffness parameters. Taking C_{11}^{sat} as an example

$$
C_{11}^{sat} = (\lambda+2\mu)(1-\Delta_{\mathrm{N}}) + \frac{K_0\left[(1-\frac{K_d}{K_0})^2 + 2(1-\frac{K_d}{K_0})\frac{K_d}{K_0}\Delta_{\mathrm{N}} + (\frac{K_d}{K_0}\Delta_{\mathrm{N}})^2\right]}{\frac{K_0}{K_f}\phi + (1-\frac{A}{K_0}-\phi)}. \tag{3}
$$

Usually the bulk modulus of fluid, K_f , is less than the effective bulk modulus of mineral, K_0 . We may assume that

$$
0 < 1 - \frac{A}{K_0} - \phi \ll \frac{A}{K_0}\phi. \tag{4}
$$

Ignoring the term, $1-\dfrac{A}{K_0}-\phi$, in the denominator and the high order of fracture weaknesses, $(\Delta_{\mathrm{N}})^2$, in the numerator yields

$$
C_{11}^{sat} = (\lambda+2\mu)(1-\Delta_{\mathrm{N}}) + \frac{(1-\frac{K_d}{K_0})^2 + 2(1-\frac{K_d}{K_0})\frac{K_d}{K_0}\Delta_{\mathrm{N}}}{\phi)}K_f. \tag{5}
$$

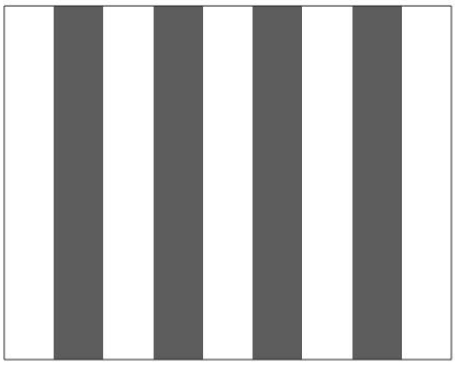

FIG. 1. A diagram of Voigt medium

Under the assumption that an HTI medium can be considered as a Voigt medium (Figure 1), the relationships between the modulus of dry rock and porosity are defined as

$$\begin{aligned} K_d &= K_0(1-\phi) \\ \mu &= \mu_0(1-\phi), \end{aligned} \tag{6}$$

where μ_0 is shear modulus of the mineral making up the rock.

Substituting equation (6) into equation (5), we further simplify equation (5) as

$$C_{11}^{sat} = (\lambda + 2\mu)(1 - \Delta_{\mathrm{N}}) + f + 2\Delta_{\mathrm{N}} K_f - 2f\Delta_{\mathrm{N}}. \tag{7}$$

where f is the Gassmann fluid term.

Figure 2 shows the fluid term variation with porosity. We can see that the fluid term increases with water saturation and porosity, which means the fluid term shows a low value for the case of gas-saturated rock.

For other stiffness parameters, C_{12}^{sat} , C_{23}^{sat}, and C_{33}^{sat} , the simplified expressions are

$$\begin{aligned} C_{12}^{sat} &= \lambda(1 - \Delta_{\mathrm{N}}) + f + (\chi + 1)\Delta_{\mathrm{N}} K_f - (\chi + 1) f\Delta_{\mathrm{N}}, \\ C_{23}^{sat} &= \lambda(1 - \chi\Delta_{\mathrm{N}}) + f + 2\chi\Delta_{\mathrm{N}} K_f - 2\chi f\Delta_{\mathrm{N}}, \\ C_{33}^{sat} &= (\lambda + 2\mu)(1 - \chi^2\Delta_{\mathrm{N}}) + f + 2\chi\Delta_{\mathrm{N}} K_f - 2\chi f\Delta_{\mathrm{N}}. \end{aligned} \tag{8}$$

In order to verify the accuracy of our simplified equations, we construct a numerical fractured rock model, and use equations (7)-(8) and equation (2) to calculate the stiffness parameters respectively. We assume the minerals making up the rock are quartz and clay, and the volumes are 0.1 and 0.9. The effective bulk modulus of minerals, K_0 , is calculated by using the Voigt-Reuss-Hill average method (Mavko et al. 2009). The fluid in the rock is the mixture of gas and brine.

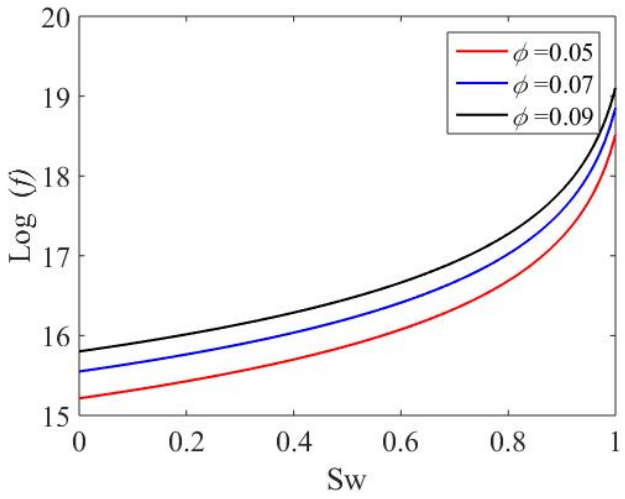

FIG. 2. Fluid term variation with porosity and water saturation

Bakulin et al. (2000) present equations for calculating the normal and tangential fracture weaknesses

$$\begin{aligned} \Delta_{\mathrm{N}} &= \frac{4e}{3g_d(1-g_d)}, \\ \Delta_{\mathrm{T}} &= \frac{16e}{3(3-2g_d)}, \end{aligned} \tag{9}$$

where g_d is velocity ratio of dry rock, and e is fracture density.

The calculated stiffness parameters are shown in Figure 3. We can see that differences between stiffness parameters calculated by equation (2) and equations (7)-(8) decreases as the gas saturation increase, which means our derived equations can be used in the gas-bearing reservoir that has a low porosity.

For the case of an interface separating two HTI media (Figure 4), the perturbation of C_{11}^{sat} across the interface is given by

$$\begin{aligned} C_{11}^{sat} =& \Delta M - (M\delta_{\Delta_{\mathrm{N}}} + \Delta M\Delta_{\mathrm{N}} + \Delta M\delta_{\Delta_{\mathrm{N}}}) \\ &+ \Delta f + 2(\Delta_{\mathrm{N}}\Delta K_f + \delta_{\Delta_{\mathrm{N}}}K_f + \delta_{\Delta_{\mathrm{N}}}\Delta K_f). \\ &\approx \Delta M - M\delta_{\Delta_{\mathrm{N}}} + \Delta f + 2(\Delta_{\mathrm{N}}\Delta K_f + \delta_{\Delta_{\mathrm{N}}}K_f) \end{aligned} \tag{10}$$

For other stiffness parameters, the perturbations are expressed as

$$\begin{aligned} C_{12}^{sat} &= \Delta\lambda - \lambda\delta_{\Delta_{\mathrm{N}}} + \Delta f + (\chi+1)\Delta_{\mathrm{N}}\Delta K_f + (\chi+1)K_f\delta_{\Delta_{\mathrm{N}}}, \\ C_{23}^{sat} &= \Delta\lambda - \lambda\chi\delta_{\Delta_{\mathrm{N}}} + \Delta f + 2\chi\Delta_{\mathrm{N}}\Delta K_f + 2\chi K_f\delta_{\Delta_{\mathrm{N}}}, \\ C_{33}^{sat} &= \Delta M - M\chi^2\delta_{\Delta_{\mathrm{N}}} + \Delta f + 2\chi\Delta_{\mathrm{N}}\Delta K_f + 2\chi K_f\delta_{\Delta_{\mathrm{N}}}, \end{aligned} \tag{11}$$

where ΔM, $\Delta\mu$, $\delta_{\Delta_{\mathrm{N}}}$, $\delta_{\Delta_{\mathrm{T}}}$, $\Delta\phi$, and ΔK_f are changes in P-wave modulus, shear modulus, the normal and tangential fracture weaknesses, porosity, and fluid bulk modulus across the interface, respectively.

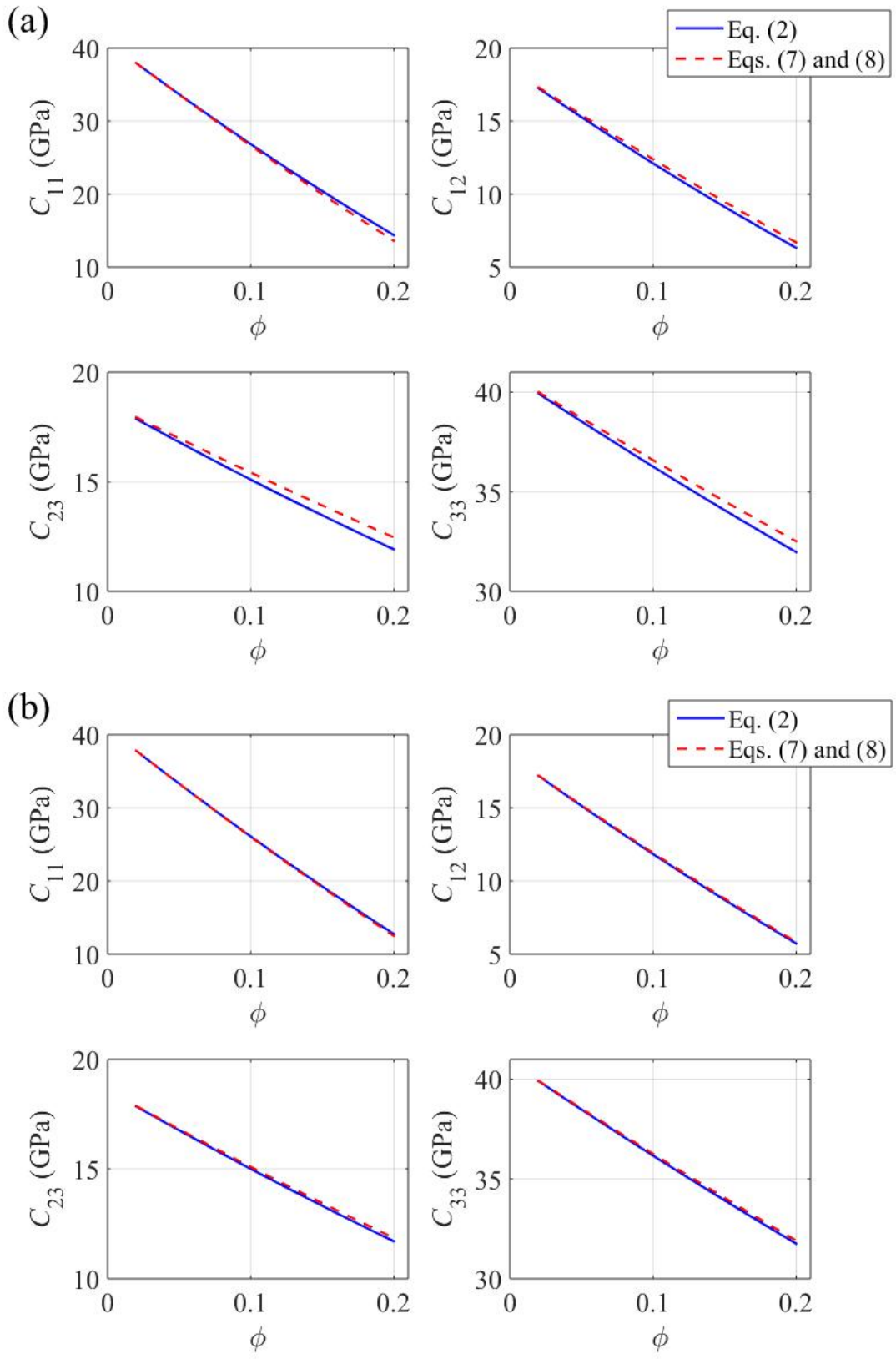

FIG. 3. Comparisons between stiffness parameters calculated by using equation (2) and equations (7)-(8). (a) gas saturation is 0.03, and (b) gas saturation is 0.2.

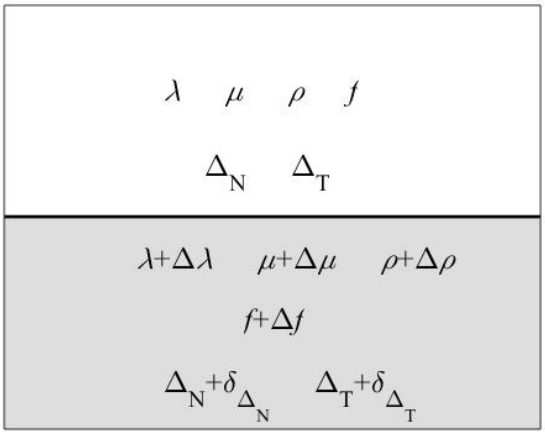

FIG. 4. Comparisons between stiffness parameters calculated by using equation (2) and equations (7)-(8). (a) gas saturation is 0.03, and (b) gas saturation is 0.2.

Under the assumption that changes in elastic parameters across the interface are small and the anisotropy is weak, we ignore the effects of $f\Delta_{\rm N}$, $\Delta M\Delta_{\rm N}$, $\Delta M\delta_{\Delta_{\rm N}}$, $\Delta\lambda\Delta_{\rm N}$, $\delta_{\Delta_{\rm N}}\Delta K_f$, $\Delta\mu\Delta_{\rm T}$, and $\Delta\mu\delta_{\Delta_{\rm T}}$ in the derivation of perturbations.

We construct a two-layer numerical model to test the accuracy of our derived perturbations. For the upper layer 1, we assume the total porosity (ϕ) is 0.08 and water saturation is 1. For the lower layer 2, the total porosity (ϕ) changes from 0.02 to 0.1, and water saturation is 0.8. Here fracture density (e) is half of the total porosity. The volumes of minerals (quartz and clay) are shown in Table 1. The calculated stiffness parameter perturbations are displayed in Figure 5.

From Figure 5, we can see that the difference between the perturbation of stiffness parameter (red) and the change in stiffness parameter across the interface (blue) is small in the case that the total porosity is less than 0.1, which indicates that our derived perturbations can be used in a fractured shale gas reservoir which has a low porosity.

Table 1. Parameters of the two-layer numerical model.

Model	Quartz	Clay	Sw	ϕ	e
Layer 1	0.1	0.9	1	0.08	0.04
Layer2	0.1	0.9	0.8	0.02 0.1	0.01 0.05

Linearized PP-wave reflection coefficient and azimuthal elastic impedance parameterization

Using the first-order perturbation of the medium parameter, Shaw and Sen (2004) evaluate the Born integral to derive a linearized expression for PP- wave reflection coefficient. Following Shaw and Sen (2004), we use the perturbation of stiffness parameter, equations (10) and (11), to derive a linearized PP- wave reflection coefficient for the saturated frac-

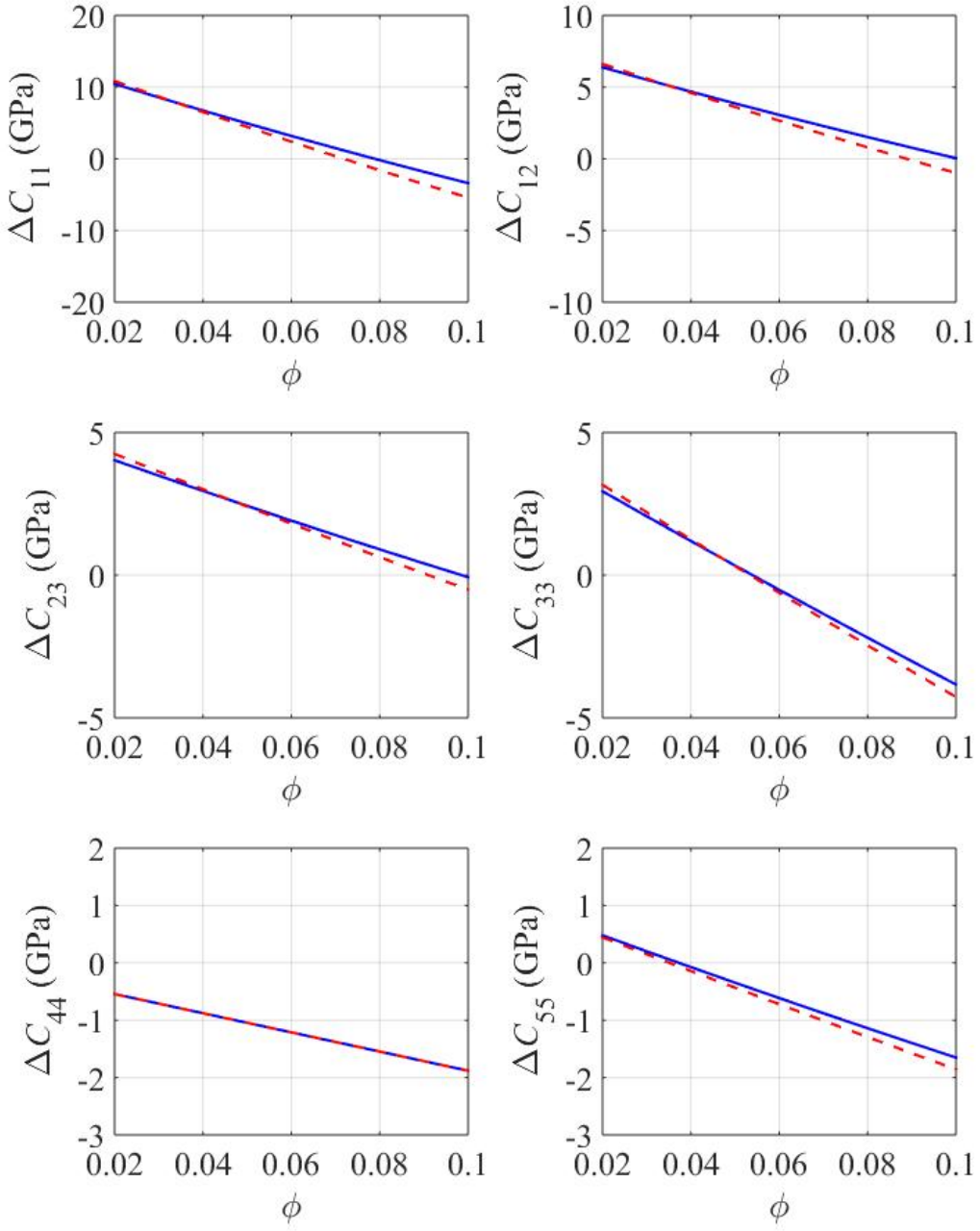

FIG. 5. Perturbations of stiffness parameters. The blue line represents the stiffness parameter difference between two layers, and the stiffness parameter is calculated by using equation (2) for each layer. The red dashed line is the stiffness parameter perturbation which is calculated using equations (10) and (11).

tured medium

$$R_{PP} = \frac{1}{4\rho\cos^2\theta}(\Delta\rho\xi + \Delta C\eta), \tag{12}$$

where θ is P-wave incident angle, ΔC is the stiffness matrix perturbation, ρ is the density of the reference medium, $\Delta\rho$ is the density perturbation, $\xi = \mathrm{t_i t_i^{'}}$, and $\eta = \mathrm{t_i^{'} p_j^{'} t_k p_l}$. In addition, p and t represent the slowness and polarization vectors. The primed quantities denote the reflective wave.

The linearized PP-wave reflection coefficient is expressed as

$$\begin{aligned} R_{PP}(\theta,\varphi) = a_{\lambda_d}(\theta)\frac{\Delta\lambda_d}{\lambda} + a_{\mu}(\theta)\frac{\Delta\mu}{\mu} + a_{\rho}(\theta)\frac{\Delta\rho}{\rho} \\ + a_f(\theta)\frac{\Delta f}{f} + a_{\Delta_\mathrm{N}}(\theta,\varphi)\delta_{\Delta_\mathrm{N}} + a_{\Delta_\mathrm{T}}(\theta,\varphi)\delta_{\Delta_\mathrm{T}}, \end{aligned} \tag{13}$$

where $a_{\lambda_d}(\theta) = \dfrac{1}{4\cos^2\theta}$, $a_{\mu}(\theta) = \dfrac{1}{4\cos^2\theta} - 2g_s\sin^2\theta$, $a_{\rho}(\theta) = \dfrac{\cos 2\theta}{4\cos^2\theta}$, $a_f(\theta) = \dfrac{1}{4\cos^2\theta}(1-\dfrac{g_s}{g_d})$, $a_{\Delta_\mathrm{N}}(\theta,\varphi) = -\dfrac{1}{4\cos^2\theta}\dfrac{g_s}{g_d}[1-2g_d(\sin^2\theta\sin^2\varphi+\cos^2\theta)]^2$, and $a_{\Delta_\mathrm{T}}(\theta,\varphi) = -g_s\tan^2\theta\cos^2\varphi(\sin^2\theta\sin^2\varphi - \cos^2\theta)$. In addition, φ is the azimuth, $\dfrac{\Delta\lambda}{\lambda}$ and $\dfrac{\Delta\mu}{\mu}$ are Lamé constant reflectivities of the dry rock, $\dfrac{\Delta\rho}{\rho}$ is the density reflectivity, $\dfrac{\Delta f}{f}$ is the Gassmann fluid term reflectivity, $g_s = \dfrac{\mu}{M_s}$, $g_d = \dfrac{\mu}{M_d}$, and M_s and M_d are P-wave moduli of the saturated and the dry rock, respectively.

The advantage of the derived PP-wave reflection coefficient is to isolate the effect of fracture and fluid, which may help to improve the reliability of fracture detection and fluid discrimination. The derived PP-wave reflection coefficient makes it possible to use amplitude variation with offset and azimuth (AVOA) data to invert for Lamé constant, density, Gassmann fluid term, and the normal and tangential weaknesses. However, AVOA data is severely affected by random noise, and the effect of seismic wavelet may also cause some uncertainties in the inversion.

In this study, we aim to utilize azimuthally incident-angle-stack (small, middle, and large angle of incidence) seismic data to implement the inversion, based on elastic impedance (EI).

Following Buland and Omre (2003), we may express the derived PP-wave reflection coefficient as a time- continuous function

$$\begin{aligned} R_{PP}(t,\theta,\varphi) =& \frac{\partial}{\partial t}\ln\mathrm{EI}(t,\theta,\varphi) \\ =& a_{\lambda_d}(t,\theta)\frac{\partial}{\partial t}\ln\lambda_\mathrm{d}(t) + a_{\mu}(t,\theta)\frac{\partial}{\partial t}\ln\mu(t) + a_{\rho}(t,\theta)\frac{\partial}{\partial t}\ln\rho(t) \\ &+ a_f(t,\theta)\frac{\partial}{\partial t}\ln f(t) + a_{\Delta_\mathrm{N}}(t,\theta,\varphi)\frac{\partial}{\partial t}\Delta_\mathrm{N}(t) + a_{\Delta_\mathrm{T}}(t,\theta,\varphi)\frac{\partial}{\partial t}\Delta_\mathrm{T}(t), \end{aligned} \tag{14}$$

where $\lambda_d(t)$, $\mu(t)$, $\rho(t)$, $f(t)$, $\Delta_{\rm N}(t)$, and $\Delta_{\rm T}(t)$ are time-dependent Lamé constants, density, Gassmann fluid term, and the normal and tangential fracture weaknesses, respectively.

We may obtain the logarithm of azimuthal EI after taking an integral operation

$$\begin{aligned}\ln{\rm EI}(t,\theta,\varphi) =& a_{\lambda_d}(t,\theta)\ln\lambda_{\rm d}(t) + a_{\mu}(t,\theta)\ln\mu(t) + a_{\rho}(t,\theta)\ln\rho(t) \\ &+ a_{f}(t,\theta)\ln f(t) + a_{\Delta_{\rm N}}(t,\theta,\varphi)\Delta_{\rm N}(t) + a_{\Delta_{\rm T}}(t,\theta,\varphi)\Delta_{\rm T}(t),\end{aligned} \tag{15}$$

The expression of azimuthal EI is given by

$$\begin{aligned}{\rm EI}(t,\theta,\varphi) =& [\lambda_{\rm d}(t)]^{a_{\lambda_d}(t,\theta)} + [\mu(t)]^{a_{\mu}(t,\theta)} + [\rho(t)]^{a_{\rho}(t,\theta)} + [f(t)]^{a_{f}(t,\theta)} \\ &\exp[a_{\Delta_{\rm N}}(t,\theta,\varphi)\Delta_{\rm N}(t) + a_{\Delta_{\rm T}}(t,\theta,\varphi)\Delta_{\rm T}(t)].\end{aligned} \tag{16}$$

Figure 6 shows the azimuthal EI variation with water saturation. Lamé constants and density are from the gas-sand model which is defined by Goodway (2001), as shown in Table 2.

Table 2. Lamé constants and density of shale model.

Parameters	λ_d (GPa)	μ (GPa)	ρ (g/cm^3)
Layer shale	12.3	4.035	2.425

We assume the shale model contains a set of vertical fractures, and fracture density (e) is half of the total porosity (ϕ), and the fluid in pore and fracture space is the mixture of gas and water. Using equation (9), we may calculate the normal and tangential fracture weaknesses. From Figure 6, we can see that the azimuthal EI decreases as the gas saturation increases.

Figure 7 shows the effect of fracture density on azimuthal EI for the case that the Gassmann fluid term remains a constant (the total porosity is 0.1, and the water saturation is 0.5). We can see that the variation of EI with azimuth becomes more obvious as fracture density increases.

Following Whitcombe (2002), we derive the normalized azimuthal EI

$$\begin{aligned}{\rm EI}(t,\theta,\varphi) =& {\rm EI}_0 \left[\frac{\lambda_d(t)}{\lambda_{d0}}\right]^{a_{\lambda_d}(t,\theta)} \left[\frac{\mu(t)}{\mu_0}\right]^{a_{\mu}(t,\theta)} \left[\frac{\rho(t)}{\rho_0}\right]^{a_{\rho}(t,\theta)} \left[\frac{f(t)}{f_0}\right]^{a_{f}(t,\theta)} \\ &\exp\left[a_{\Delta_{\rm N}}(t,\theta,\varphi)\Delta_{\rm N}(t) + a_{\Delta_{\rm T}}(t,\theta,\varphi)\Delta_{\rm T}(t)\right],\end{aligned} \tag{17}$$

where ${\rm EI}_0 = \sqrt{\rho_0(\lambda_{d0}+2\mu_0)}$. In addition, λ_{d0}, μ_0 , ρ_0 , and f_0 are constants, which may be obtained from well-logs and rock physics results.

Nonlinear Inversion of azimuthal EI for fluid term and fracture weaknesses

In order to implement the estimation of fluid term and fracture weaknesses, we demonstrate a method to predict EI from partially incident-angle-stack seismic data at different

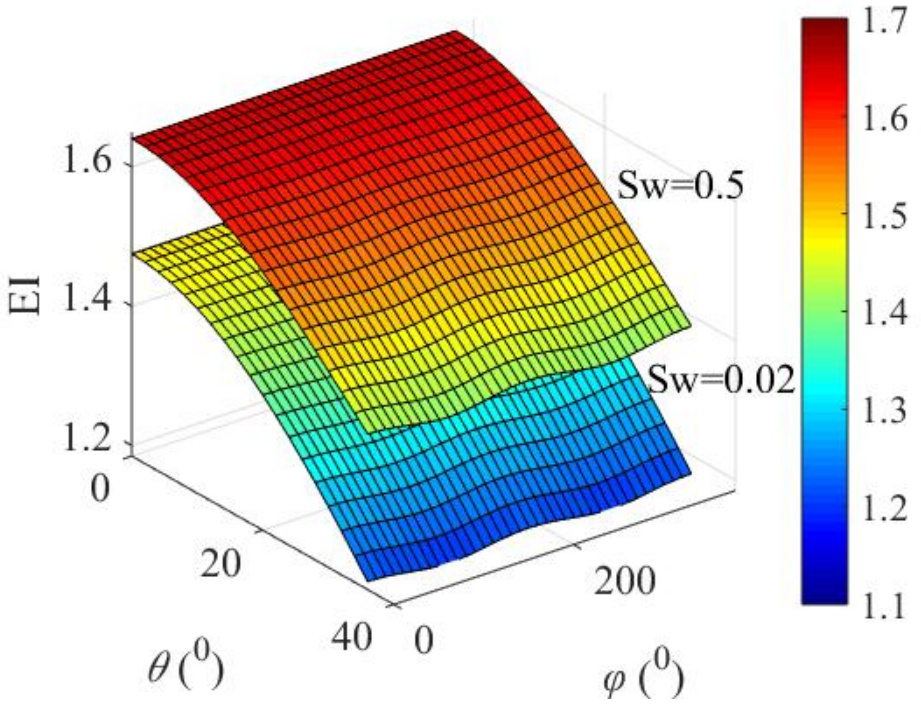

FIG. 6. EI variation with the incident angle and azimuth. The water saturation is 0.5 and 0.02, respectively.

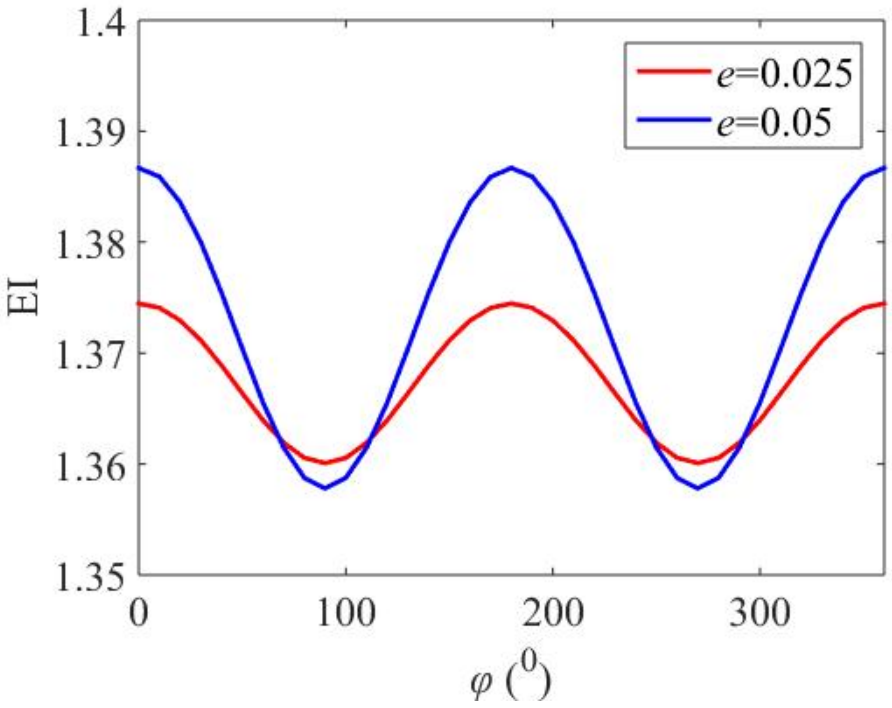

FIG. 7. EI variation with azimuth. The incident angle is 40^0.

azimuths first, and then to extract Lamé constants, density, fluid term, and the normal and tangential weaknesses from the estimated EI.

The PP- wave reflection coefficient, $R_{PP}(t,\theta,\varphi)$, can be calculated by the azimuthal EI

$$R_{PP}(t,\theta,\varphi) = \frac{1}{2}\frac{\Delta \mathrm{EI}(t,\theta,\varphi)}{\overline{\mathrm{EI}}(t,\theta,\varphi)} \approx \frac{1}{2} d\ln[\mathrm{EI}(t,\theta,\varphi)] \tag{18}$$

where $\Delta\mathrm{EI}$ and $\overline{\mathrm{EI}}$ are difference and mean values between the upper and lower layers, respectively.

Seismic traces may be generated by using the convolution model which is expressed as

$$\begin{bmatrix} S(t_1,\theta,\varphi) \\ S(t_2,\theta,\varphi) \\ \vdots \\ S(t_i,\theta,\varphi) \\ S(t_{i+1},\theta,\varphi) \\ \vdots \\ S(t_{N-1},\theta,\varphi) \\ S(t_N,\theta,\varphi) \end{bmatrix} = \begin{bmatrix} w_1 & 0 & 0 & \dots \\ w_2 & w_1 & 0 & \ddots \\ w_3 & w_2 & w_1 & \ddots \\ \vdots & \ddots & \ddots & \ddots \end{bmatrix} \begin{bmatrix} -1 & 1 & 0 & 0 & 0 & 0 \\ 0 & \ddots & \ddots & 0 & 0 & 0 \\ 0 & 0 & -1 & 1 & 0 & 0 \\ 0 & 0 & 0 & \ddots & \ddots & 0 \\ 0 & 0 & 0 & 0 & -1 & 1 \end{bmatrix} \begin{bmatrix} \mathrm{lnEI}(t_1,\theta,\varphi) \\ \mathrm{lnEI}(t_2,\theta,\varphi) \\ \vdots \\ \mathrm{lnEI}(t_i,\theta,\varphi) \\ \mathrm{lnEI}(t_{i+1},\theta,\varphi) \\ \vdots \\ \mathrm{lnEI}(t_{N-1},\theta,\varphi) \\ \mathrm{lnEI}(t_N,\theta,\varphi) \end{bmatrix}, \tag{19}$$

where is the ith time sample, and w_1, w_2, and w_3 are wavelet samples.

Equation (19) may be succinctly written as

$$B = AX, \tag{20}$$

where B represents partially incident-angle-stack seismic data, X represents the logarithm of EI, and A is the operator which includes the effect of wavelet.

The prediction of azimuthal EI results is an inversion of stack seismic data, which is implemented by using partially incident-angle-stack seismic data and wavelets at different azimuths. The least- square method is employed to solve the inverse problem to obtain the logarithm results of azimuthal EI.

Combining equation (15), we may extract Lamé constants, density, fluid term, and fracture weaknesses from the estimated logarithm results of azimuthal EI. In the present study, following a Bayesian framework, we develop a method to predict the elastic parameters (Lamé constants and density), Gassmann fluid term, and fracture weaknesses, based on Markov- chain Monte Carlo (MCMC) algorithm.

The estimation of fluid term and fracture weaknesses from azimuthal EI may be described as a nonlinear forward problem

$$d = F(m) + error, \tag{21}$$

where $error$ is the noise, d is the input data which represents the estimated azimuthal EI, $F(\cdot)$ is called the forward operator, and is the model parameter. In addition, the model

parameter is given by

$$m = (\ln\lambda_d, \ln\mu, \ln\rho, \ln f, \Delta_{\rm N}, \Delta_{\rm T}). \tag{22}$$

Bayesian theorem, which is used to calculate the posterior Probability Distribution function (PDF) from the likelihood function and a prior probability function, can be expressed as

$$P(m|d) = \frac{P(d|m)P(m)}{P(d)} \propto P(d|m)P(m), \tag{23}$$

Where $P(m|d)$ is the posterior PDF, $P(d|m)$ is the likelihood function, and $P(m)$ is the prior probability of the model parameter, respectively.

Under the assumption that the noise is independent and Gaussian (Downton, 2005), the likelihood function is written as

$$P(d|m) = \frac{1}{(2\pi\sigma_e^2)^{N/2}} \exp\left\{-\Sigma\frac{[d-G(m)]^2}{2\sigma_e^2}\right\}, \tag{24}$$

where σ_e^2 is the variance of the noise, and N is the number of the input data.

For the prior probability, Alemie and Sacchi (2011) point out that a Cauchy probability distribution has long tails and the Cauchy distribution prior information may produce sparse solutions. In our study, we assume the unknown parameter (Lamé constants, density, fluid term, and the normal and tangential fracture weaknesses) are independent of each other and use the Cauchy distribution as a prior. Hence the prior probability is given by

$$\begin{aligned} P(m) =& P(\ln\lambda_d)P(\ln\mu)P(\ln\rho)P(\ln f)P(\Delta_{\rm N})P(\Delta_{\rm T}) \\ =& \frac{1}{(2\pi\sigma_{\ln\lambda_d}^2)^{N/2}} \exp\left[-\Sigma\frac{(\ln\lambda_d - m_{\ln\lambda_d})^2}{2\sigma_{\ln\lambda_d}^2}\right] \frac{1}{(2\pi\sigma_{\ln\mu}^2)^{N/2}} \exp\left[-\Sigma\frac{(\ln\mu - m_{\ln\mu})^2}{2\sigma_{\ln\mu}^2}\right] \\ & \frac{1}{(2\pi\sigma_{\ln\rho}^2)^{N/2}} \exp\left[-\Sigma\frac{(\ln\rho - m_{\ln\rho})^2}{2\sigma_{\ln\rho}^2}\right] \frac{1}{(2\pi\sigma_{\ln f}^2)^{N/2}} \exp\left[-\Sigma\frac{(\ln f - m_{\ln f})^2}{2\sigma_{\ln f}^2}\right] \\ & \frac{1}{(2\pi\sigma_{\Delta_{\rm N}}^2)^{N/2}} \exp\left[-\Sigma\frac{(\Delta_{\rm N} - m_{\Delta_{\rm N}})^2}{2\sigma_{\Delta_{\rm N}}^2}\right] \frac{1}{(2\pi\sigma_{\Delta_{\rm T}}^2)^{N/2}} \exp\left[-\Sigma\frac{(\Delta_{\rm T} - m_{\Delta_{\rm T}})^2}{2\sigma_{\Delta_{\rm T}}^2}\right], \end{aligned} \tag{25}$$

where $m_{\ln\lambda_d}$, $m_{\ln\mu}$, $m_{\ln\rho}$, $m_{\ln f}$, $m_{\Delta_{\rm N}}$, and $m_{\Delta_{\rm T}}$ are mean values of the unknown parameters, and $\sigma_{\ln\lambda_d}^2$, $\sigma_{\ln\mu}^2$, $\sigma_{\ln\rho}^2$, $\sigma_{\ln f}^2$, $\sigma_{\Delta_{\rm N}}^2$, and $\sigma_{\Delta_{\rm T}}^2$ are variance values.

Substituting equations (24) and (25) into equation (23), we may obtain the posterior PDF

$$\begin{aligned} P(m|d) =& \frac{1}{(2\pi\sigma_{\ln\lambda_d}^2)^{N/2}} \frac{1}{(2\pi\sigma_{\ln\mu}^2)^{N/2}} \frac{1}{(2\pi\sigma_{\ln\rho}^2)^{N/2}} \\ & \frac{1}{(2\pi\sigma_{\ln f}^2)^{N/2}} \frac{1}{(2\pi\sigma_{\Delta_{\rm N}}^2)^{N/2}} \frac{1}{(2\pi\sigma_{\Delta_{\rm T}}^2)^{N/2}} \exp\left[g(x)\right], \end{aligned} \tag{26}$$

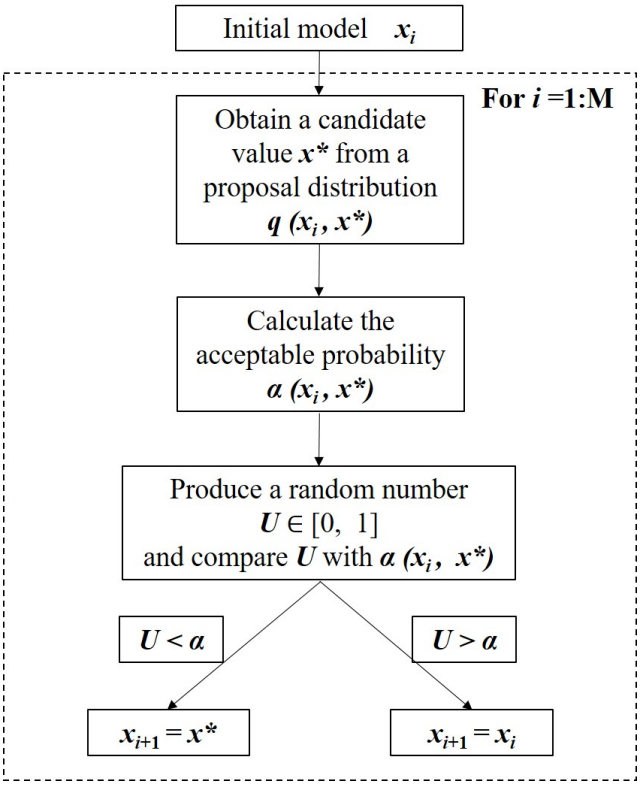

FIG. 8. The detailed procedure of Metropolis- Hastings algorithm. The parameter M is the number of the iteration.

where

$$g(x) = -\Sigma\frac{(\ln\lambda_d - m_{\ln\lambda_d})^2}{2\sigma^2_{\ln\lambda_d}} - \Sigma\frac{(\ln\mu - m_{\ln\mu})^2}{2\sigma^2_{\ln\mu}} - \Sigma\frac{(\ln\rho - m_{\ln\rho})^2}{2\sigma^2_{\ln\rho}}$$
$$- \Sigma\frac{(\ln f - m_{\ln f})^2}{2\sigma^2_{\ln f}} - \Sigma\frac{(\Delta_{\mathrm{N}} - m_{\Delta_{\mathrm{N}}})^2}{2\sigma^2_{\Delta_{\mathrm{N}}}} - \Sigma\frac{(\Delta_{\mathrm{T}} - m_{\Delta_{\mathrm{T}}})^2}{2\sigma^2_{\Delta_{\mathrm{T}}}} - \Sigma\frac{[d - G(m)]^2}{2\sigma_e^2}.$$

The Metropolis- Hastings algorithm is employed in our study, which includes two main steps. The first step is to obtain a candidate value x^* which is drawn from a proposal distribution $q(x, x^*)$, based on an initial information x. The second step is to find the candidate value which meets an acceptable probability $\alpha(x, x^*)$. Figure 8 shows the detailed procedure of Metropolis- Hastings algorithm.

The acceptable probability $\alpha(x, x^*)$ is calculated by assuming that the proposal distribution $q(x, x^*)$ obeys a symmetric distribution, i.e. $q(x, x^*) = q(x^*, x)$.

$$\alpha(x, x^*) = \min\left[1, \frac{\pi(x^*)q(x^*, x)}{\pi(x)q(x, x^*)}\right] = \min\left[1, \frac{\pi(x^*)}{\pi(x)}\right], \tag{27}$$

where $\pi(\cdot)$ denotes the stationary distribution.

The stationary distribution $\pi(\cdot)$ should be equal to the posterior probability $P(m|d)$ to find the value which is convergent to the posterior probability. Hence the acceptable

probability is expressed as

$$\alpha(x, x^*) = \exp\{\min[0, g(x^*) - g(x)]\}. \tag{28}$$

EXAMPLES

Synthetic test

Azimuthally synthetic seismic data, which are generated by using well- logs, a 40HZ Ricker wavelet, and the convolutional model, based on equations (16) and (19), are used to verify the proposed inversion method. Azimuths (φ) of synthetic data are 0^0, 30^0, 60^0, and 90^0. The incident angle range is $0^0 \sim 30^0$, and the stack central angles are $5^0(0^0 \sim 10^0)$, $15^0(10^0 \sim 20^0)$, and $25^0(20^0 \sim 30^0)$.

In order to obtain well- log curves of Lamé constants, Gassmann fluid term, and fracture weaknesses, Gassmann equation and an anisotropic rock physics effective model are employed (Chen et al. 2016). A random noise, which obeys the Gaussian distribution, is added to synthetic seismic data to test the robustness of the inversion method.

Figure 9 shows the comparison between true values (blue) and inverted results (red) of well- log data, which indicates that the proposed inversion method can obtain a reasonable result when seismic data contain a moderate noise.

Inversion of real data

Partially incident-angle-stack real data, which are from a fractured shale reservoir, are utilized to test the reliability of our nonlinear inversion method. The real data are processed to ensure that the seismic amplitude may image the effect of elastic properties, fluid, and fracture weaknesses across the interface as correctly as possible.

Figure 10 shows the stack seismic profiles. The blue line represents the location of well A, and there is an abnormal strong amplitude in the circle. The drilling and well- log results shows this is the response of a gas- bearing reservoir. The comparison between azimuths indicates that the amplitude also varies with the azimuth, which may reveal the azimuthal anisotropy of the reservoir.

The inverted results of azimuthal EI are displayed in Figure 11. We can see that the inverted azimuthal EI shows low values in the location of the circle. Using the inverted azimuthal EI, we may implement the estimation of Lamé constants, density, fluid term, and the normal and tangential fracture weaknesses with the proposed Bayesian MCMC inversion method.

The estimated Lamé constants, density, fluid term, and the normal and tangential fracture weaknesses are shown in Figure 12. For the gas- bearing reservoir (the location of the circle), the estimated Lamé constants and fluid term show low values, and the normal and tangential fracture weaknesses show high values, which means the reservoir contains a few vertical or sub-vertical fractures.

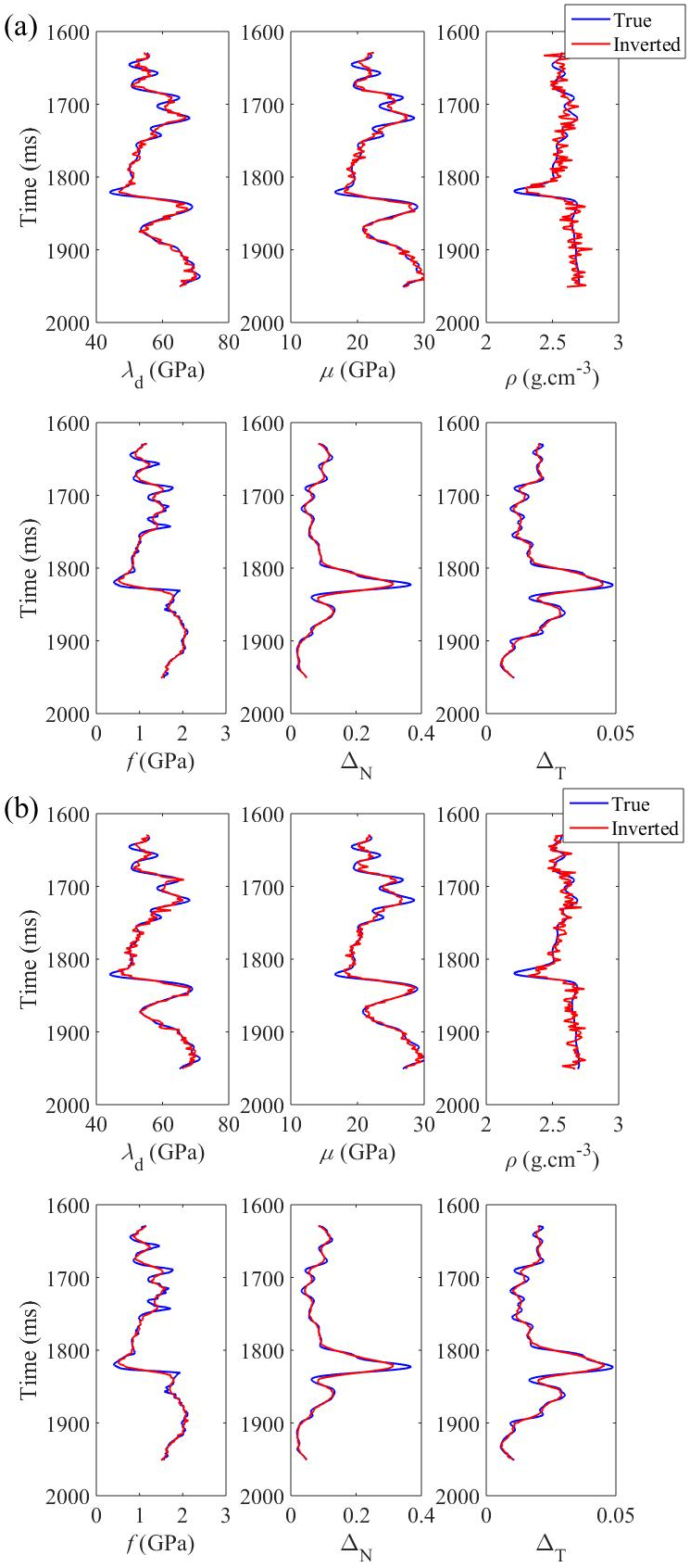

FIG. 9. Comparisons between true values (blue) and inverted results (red) of well- log data. (a) SNR=5, and (b) SNR=1

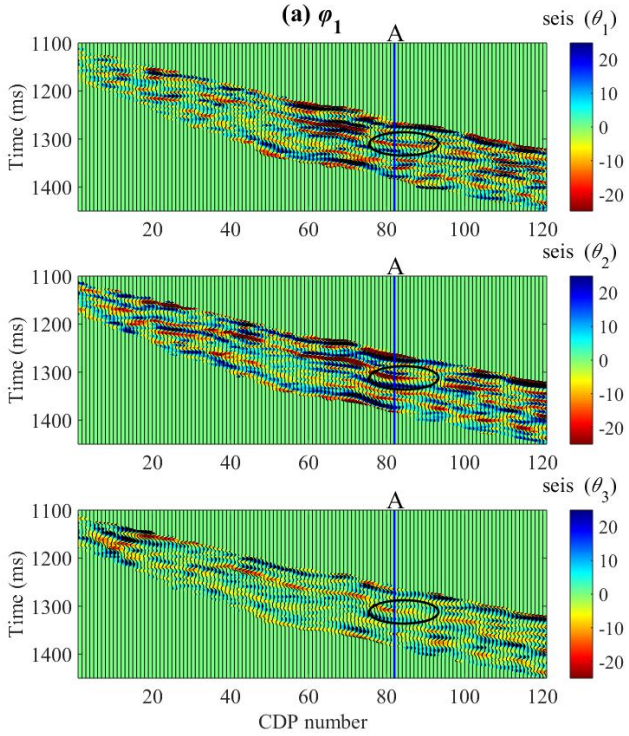
(a) φ_1
seis (θ_1)
seis (θ_2)
seis (θ_3)
A
Time (ms)
1100
1200
1300
1400
20
40
60
80
100
120
CDP number
20
10
0
-10
-20

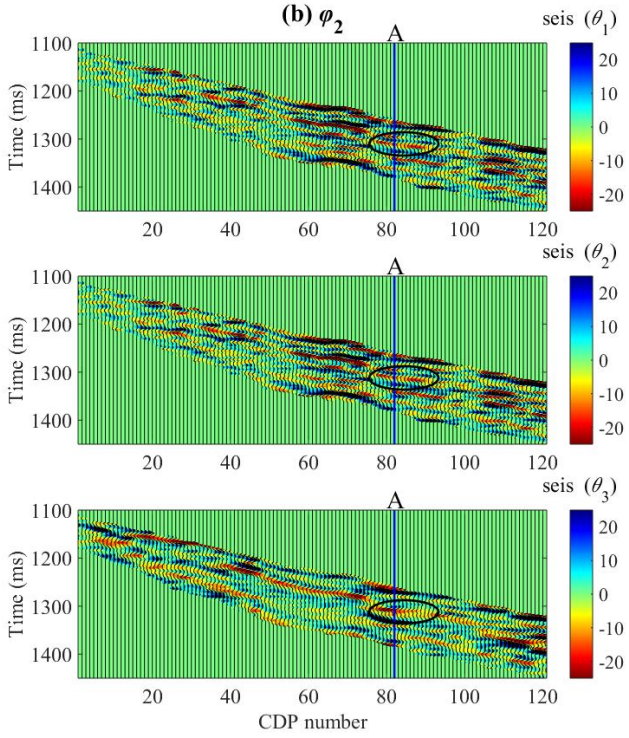
(b) φ_2
seis (θ_1)
seis (θ_2)
seis (θ_3)
A
Time (ms)
1100
1200
1300
1400
20
40
60
80
100
120
CDP number
20
10
0
-10
-20

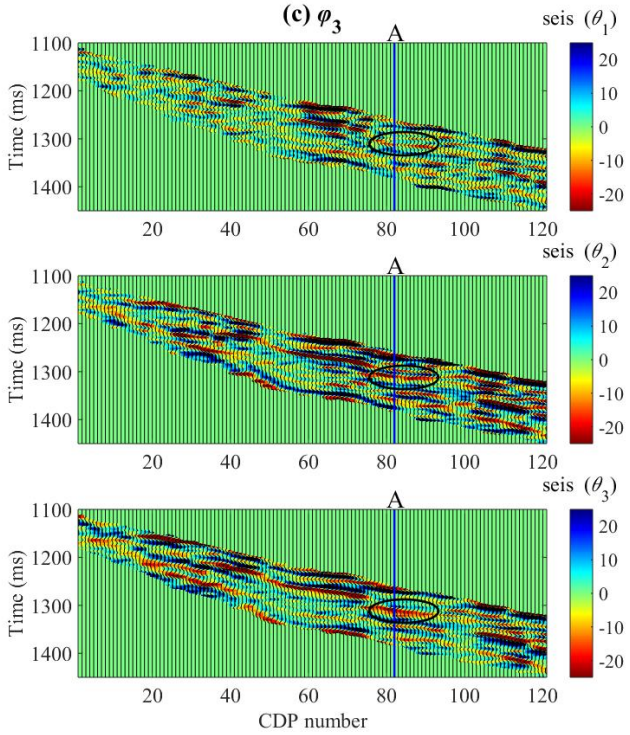

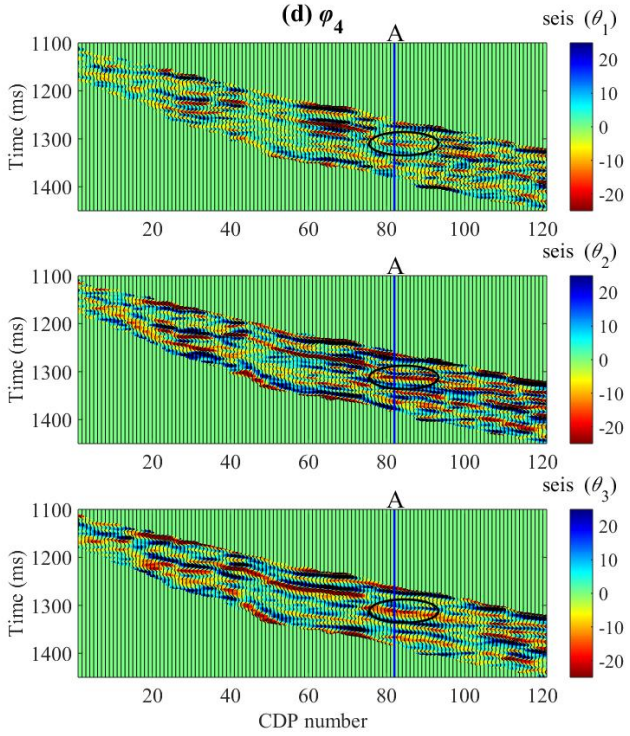

FIG. 10. Partially incident-angle-stack seismic profiles. The azimuths $\varphi_1 = 0^0$, $\varphi_2 = 30^0$, $\varphi_3 = 60^0$, and $\varphi_4 = 90^0$, and the incident angles $\theta_1 = 8^0$, $\theta_2 = 16^0$, and $\theta_3 = 24^0$.

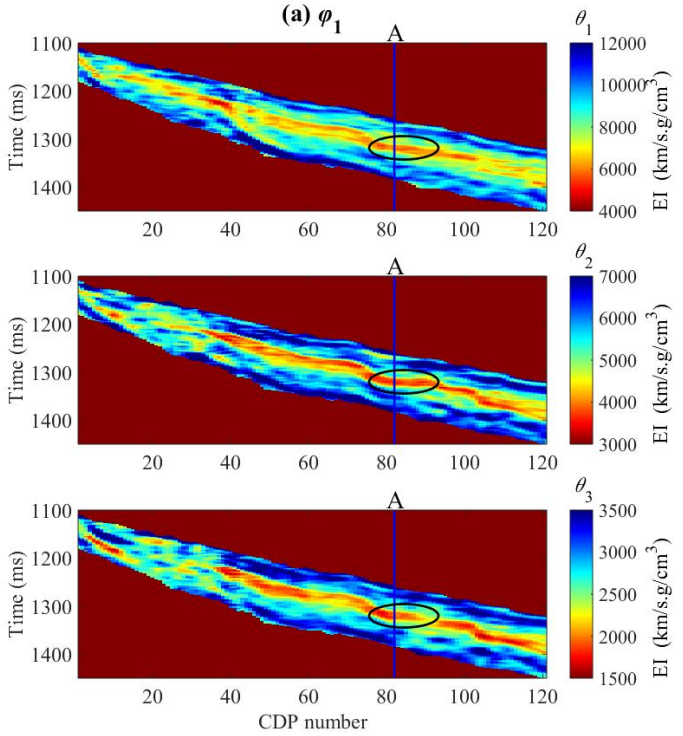
(a) φ_1
A
θ_1
θ_2
θ_3
Time (ms)
CDP number
EI (km/s.g/cm^3)

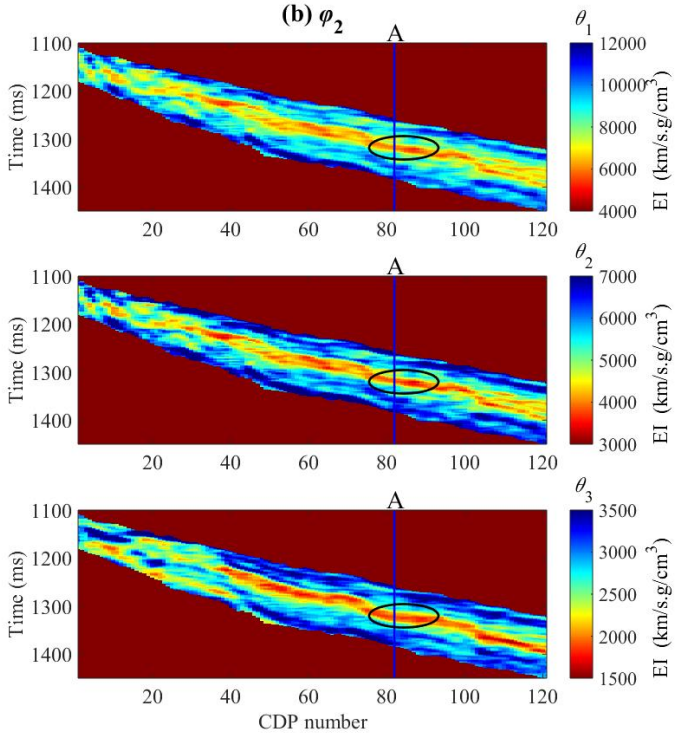
(b) φ_2
A
θ_1
θ_2
θ_3
Time (ms)
CDP number
EI (km/s.g/cm^3)

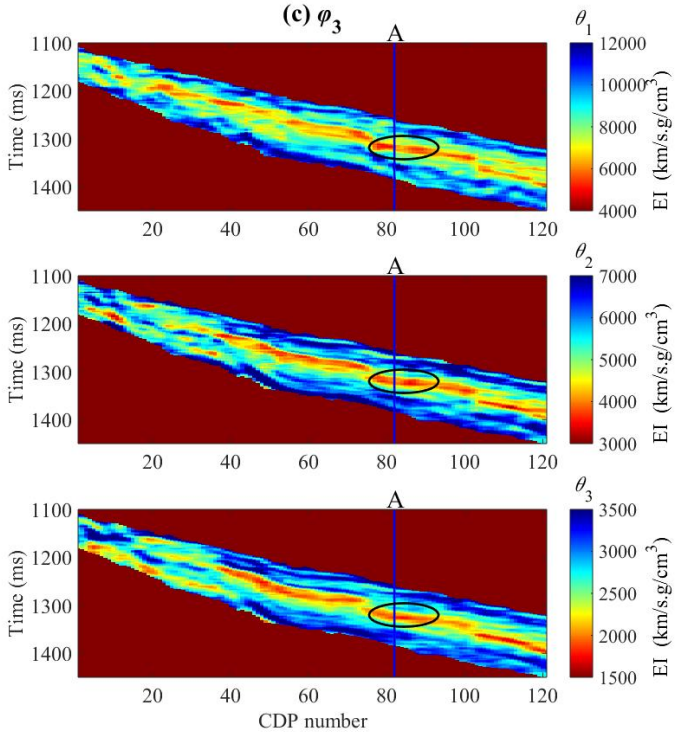

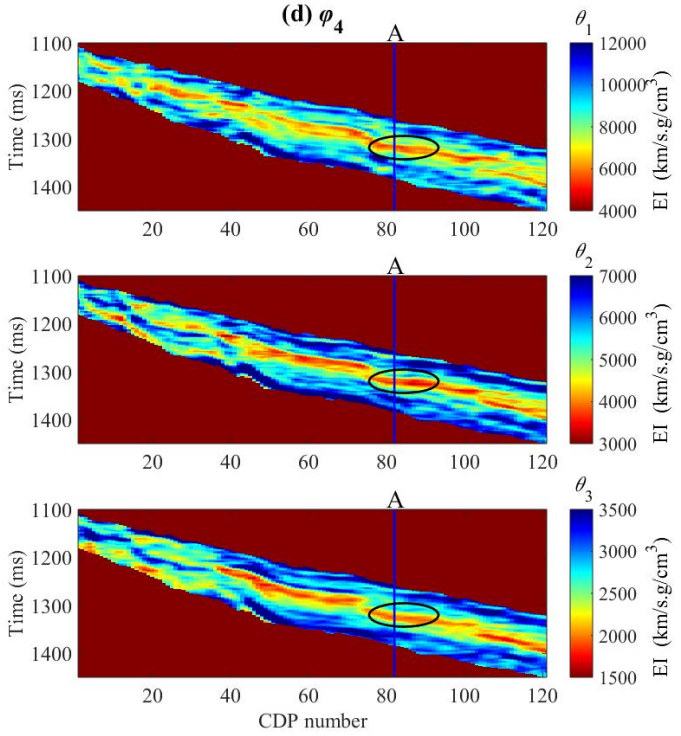

FIG. 11. Partially incident-angle-stack seismic profiles. The azimuths $\varphi_1 = 0^0$, $\varphi_2 = 30^0$, $\varphi_3 = 60^0$, and $\varphi_4 = 90^0$, and the incident angles $\theta_1 = 8^0$, $\theta_2 = 16^0$, and $\theta_3 = 24^0$.

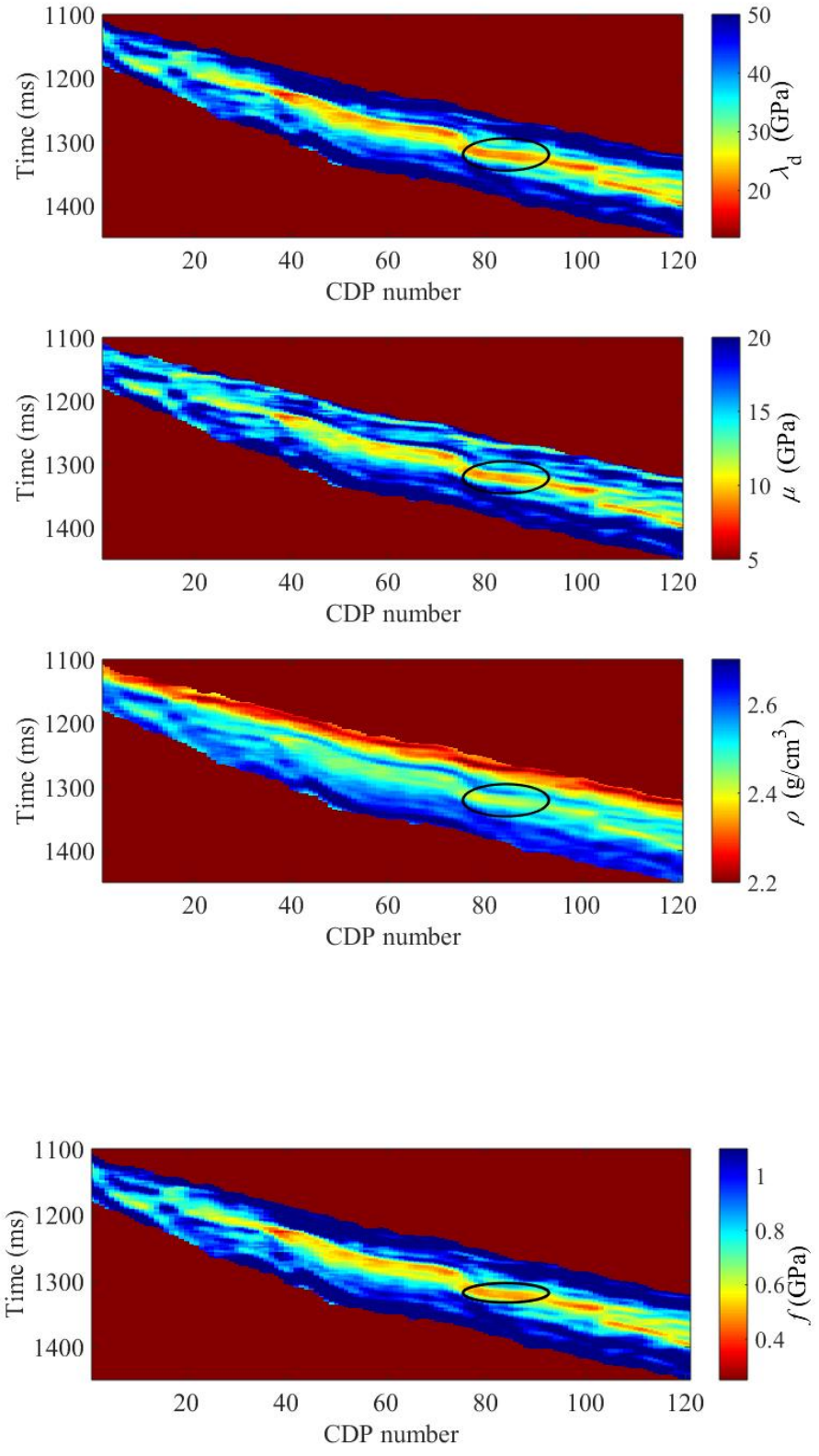
Time (ms)
1100
1200
1300
1400
20
40
60
80
100
120
CDP number
50
40
30
20
λ_d (GPa)
20
15
10
5
μ (GPa)
2.6
2.4
2.2
ρ (g/cm^3)
1
0.8
0.6
0.4
f(GPa)

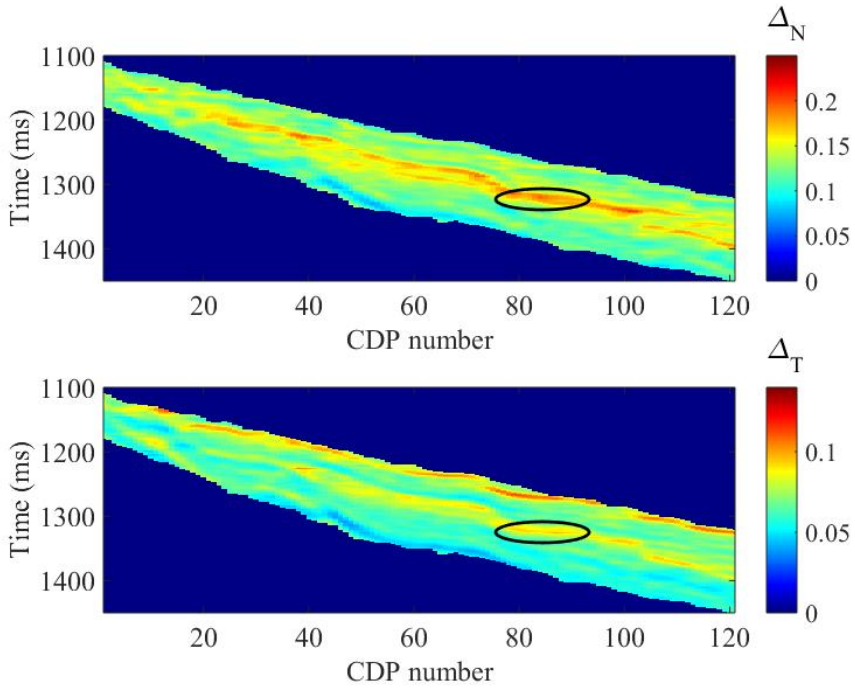

FIG. 12. Inverted results of Lamé constants, density, fluid term, and the normal and tangential fracture weaknesses.

We use the inverted results and extracted wavelets to generate synthetic seismic traces with the convolution model and equations (17)-(19) for the case that the angle of incidence is 8^0. Figure 13 show the comparison between the synthetic traces and the corresponding real data. We can see that the synthetic traces match the real data well, which may verify the accuracy of the proposed inversion method.

DISCUSSION

We derive a few simplified equations for fluid substitution in HTI media, based on the Gassmann equation for anisotropic media and Huang et al. (2015) equation. In the derivation, assumptions we use include the small fracture weaknesses and low-moduli fillings, which means the normal and tangential fracture weaknesses are not too large and the filling is fluid. Hence out equations are reasonable when they are used in a weak anisotropic fluid saturated medium.

For real data processing, the estimation of fracture symmetry azimuth is required. The method we use to estimate the fracture symmetry azimuth is AVOA analysis (Chen et al. 2016). In our real data test, the azimuth is the result which has been removed the effect of the fracture symmetry azimuth.

Reasonable initial models are important for producing and obtaining Markov chains to find acceptable solutions of unknown parameters. Interpretation results of well logs (porosity, minerals, fluid, saturation, etc.) can be used to construct initial models of Lamé constants, density, and Gassmann fluid term, based on rock physic analysis. Combining

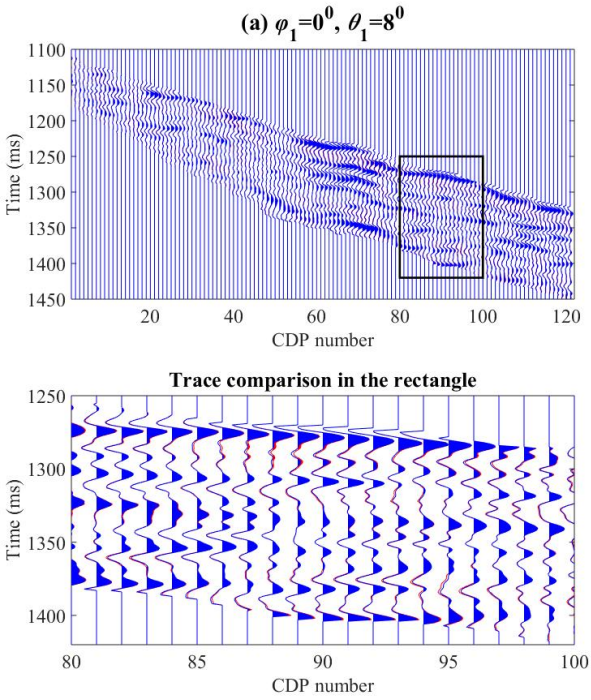
(a) $\varphi_1=0^0$, $\theta_1=8^0$
Time (ms)
CDP number
Trace comparison in the rectangle
Time (ms)
CDP number

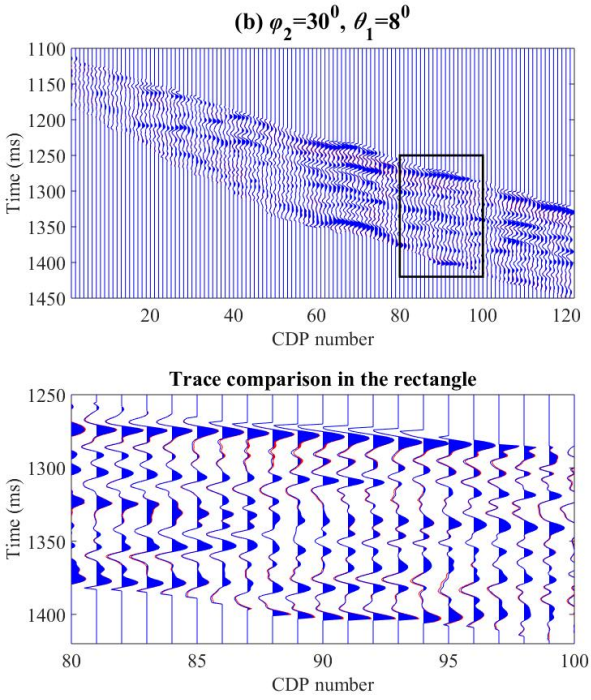
(b) $\varphi_2=30^0$, $\theta_1=8^0$
Time (ms)
CDP number
Trace comparison in the rectangle
Time (ms)
CDP number

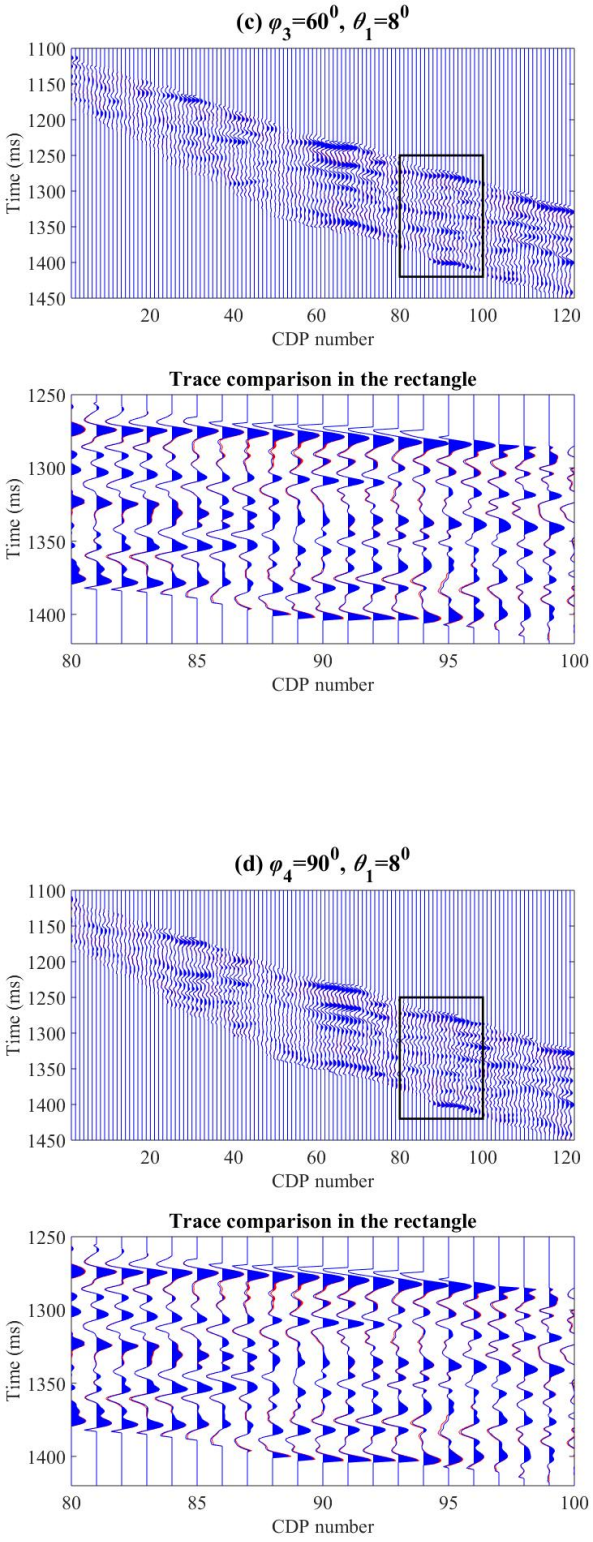

FIG. 13. Comparisons between synthetic traces (blue) and real data (red). The synthetic trace are generated by using the inverted results and the extracted wavelet.

equation (9), the analysis of imaging well log and cores may obtain fracture density, and then produce initial models of fracture weaknesses.

CONCLUSIONS

We demonstrate a method to estimate fluid term and fracture weaknesses from azimuthally seismic data, based on azimuthal elastic impedance (EI) parameterization and inversion. From the simplification and approximation of Gassmann equations for fluid substitution in HTI media, we propose the perturbation of stiffness parameters for an interface separating two HTI media. Numerical models of gas- bearing fractured shale are used to verify the accuracy of the approximation and simplification. Combing the scattering function, we derive a linearized expression of PP- wave reflection coefficient in terms of Lamé constants, density, Gassmann fluid term, and the normal and tangential fracture weaknesses, which can isolate the effects of the isotropic dry rock framework, fluid, and fractures. Using the derived PP- wave reflection coefficient, we present the expression of azimuthal EI and its normalization. Based on the azimuthal EI, we demonstrate a method to predict Gassmann fluid term and fracture weaknesses from azimuthally seismic data. The prediction is implemented as a two-step inversion, which includes partially incident-angle-stack seismic data inversion for azimuthal EI using a least- square method, and the estimation of Lamé constants, density, fluid term, and fracture weaknesses from the inverted azimuthal EI with a Bayesian MCMC inversion algorithm. Synthetic seismic traces (SNRs are 5, and 2, respectively) and real data are utilized to verify the stability of our inversion method. Synthetic tests indicates that our method may obtain a reasonable result when seismic data contain a moderate noise. The real data test shows that the inverted Lamé constants and Gassmann fluid term show low values and fracture weaknesses show high values in the location of a gas-bearing fractured shale reservoir, which confirms that our inversion is useful for fluid identification and fracture detection.

ACKNOWLEDGEMENTS

We thank the sponsors of CREWES for their support. We gratefully acknowledge support from NSERC (Natural Science and Engineering Research Council of Canada). We also thank the support from SINOPEC Key Lab of Multi-Component Seismic Technology.

REFERENCES

Bachrach, R., Sengupta, M., Salama, A., et al., 2009, Reconstruction of the layer anisotropic elastic parameter and high resolution fracture characterization from P-wave data: a case study using seismic inversion and Bayesian rock physics parameter estimation: Geophysical Prospecting, 57, 253-262.

Bakulin, A., Grechka,V., and Tsvankin, I., 2000, Estimation of fracture parameters from reflection seismic data -Part I: HTI model due to a single fracture set: Geophysics, 65(6), 1788-1802.

Buland, A., and More, H., 2003, Bayesian linearized AVO inversion: Geophysics, 68, 185-198.

Chen, H., Yin, X., Qu, S., and Zhang, G., 2014a, AVAZ inversion for fracture weakness parameters based on the rock physics model: Journal of Geophysics and Engineering, 11, 065007.

Chen, H., Zhang, G., Chen, J., and Yin, X., 2014b, Fracture filling fluids identification using azimuthally elastic impedance based on rock physics: Journal of Applied Geophysics, 110, 98-105.

Chen, H., Zhang, G., Ji, Y., and Yin, X., 2016, Azimuthal seismic difference inversion for fracture weakness: Pure and applied geophysics, in press.

Downton, J., and Roure, B., 2010, Azimuthal simultaneous elastic inversion for fracture detection: SEG Technical Program Expanded Abstracts, 263-267.

Gassmann, F., 1951, Uber die elastizitat poroser medien: Viertel. Naturforsch. Ges. ZÃijrich, 96, 1-23.

Goodway, B., Chen, T., and Downton, J., 1997, Improved AVO fluid detection and lithology discrimination using Lamé petrophysical parameters; $\lambda\rho$,$\mu\rho$, λ/μ fluid stack, from P and S inversions: SEG Technical Program Expanded Abstracts, 183-186.

Huang, L., Stewart, R., Sil, S., and Dyaur, N., 2015, Fluid substitution effects on seismic anisotropy: Journal of Geophysical Research Earth science, 120, 850-863.

Martins, J., 2006, Elastic impedance in weakly anisotropic media: Geophysics, 71, D73-D83.

Rüger, A., 1997, P-wave reflection coefficients for transversely isotropic models with vertical and horizontal axis of symmetry: Geophysics, 62, 713-722.

Schoenberg, M., and Douma, J., 1988, Elastic wave propagation in media with parallel fractures and aligned cracks: Geophysical Prospecting, 36(6), 571-590.

Schoenberg, M., and Sayers, C., 1995, Seismic anisotropy of fractured rock: Geophysics, 60(1), 204-211.

Shaw, R., and Sen, M., 2004, Born integral, stationary phase and linearized reflection coefficients in weak anisotropic media: Geophysical Journal International, 158, 225-238.

Yin, X., and Zhang, S., 2014, Bayesian inversion for effective pore-fluid bulk modulus based on fluid-matrix decoupled amplitude variation with offset approximation: Geophysics, 79, R221-R232.

Zong, Z., Yin, X., and Wu, G., 2012, AVO inversion and poroelasticity with P- and S-wave moduli, Geophysics, 77, N17-N24.